

## Article

# Exploring the Potential of Green Synthesized $\text{Sr}_{0.8}\text{Ce}_{0.2}\text{Fe}_{0.8}\text{Co}_{0.2}\text{O}_3$ Using Orange and Lemon Extracts for Hybrid Supercapacitor Applications

Asmara Fazal <sup>1,\*</sup>, M. Javaid Iqbal <sup>1,\*</sup> , Mohsin Ali Raza <sup>2</sup>, Badriah S. Almutairi <sup>3</sup>, Hesham M. H. Zakaly <sup>4,5,6</sup>, Naureen Akhtar <sup>7,\*</sup>, Muneeb Irshad <sup>8</sup> and Saira Riaz <sup>1</sup>

<sup>1</sup> Centre of Excellence in Solid State Physics, University of the Punjab, Quaid-e-Azam Campus, Lahore 54590, Pakistan

<sup>2</sup> Institute of Metallurgy and Materials Engineering, University of the Punjab, Lahore 54590, Pakistan

<sup>3</sup> Department of Physics, College of Science, Princess Nourah bint Abdulrahman University, P.O. Box 84428, Riyadh 11671, Saudi Arabia

<sup>4</sup> Institute of Physics and Technology, Ural Federal University, Yekaterinburg 620002, Russia

<sup>5</sup> Department of Physics and Technical Sciences, Western Caspian University, Baku AZ1001, Azerbaijan

<sup>6</sup> Computer Engineering Department, Faculty of Engineering and Natural Sciences, Istinye University, Istanbul 34396, Turkey

<sup>7</sup> Department of Engineering Sciences, University of Agder, 4879 Grimstad, Norway

<sup>8</sup> Department of Physics, University of Engineering and Technology, Lahore 54590, Pakistan

\* Correspondence: [asmara.phd.cssp@pu.edu.pk](mailto:asmara.phd.cssp@pu.edu.pk) (A.F.); [javid.cssp@pu.edu.pk](mailto:javid.cssp@pu.edu.pk) (M.J.I.); [naureen.akhtar@uia.no](mailto:naureen.akhtar@uia.no) (N.A.)

## Abstract

Supercapacitors are required to store energy from renewable resources to ensure a pollutant-free environment. To further encourage its study, researchers are interested in introducing green methods to produce electrode materials. Green synthesis is an innovative and emerging field because plant extracts are the best substitute for toxic chemicals. They are considered eco-friendly and cost-effective. In this work, two plant extracts, orange juice (ORJ) and lemon juice (LMJ), are used to synthesize the  $\text{Sr}_{0.8}\text{Ce}_{0.2}\text{Fe}_{0.8}\text{Co}_{0.2}\text{O}_3$  perovskite using the auto-combustion method. The electrochemical performance of  $\text{Sr}_{0.8}\text{Ce}_{0.2}\text{Fe}_{0.8}\text{Co}_{0.2}\text{O}_3$  made from LMJ and ORJ is compared to check their effectiveness. LMJ proved to be a better reducing agent than ORJ with a higher specific capacity of 300 C/g (544 F/g) at 1 A/g current density due to increased oxygen vacancies and surface area. These findings show that green-synthesized perovskites can be utilized in high-performance hybrid supercapacitor devices.

**Keywords:** hybrid supercapacitor; green synthesis; reducing agent; lemon juice; orange juice



Academic Editor: Ottorino Veneri

Received: 24 June 2025

Revised: 7 August 2025

Accepted: 9 August 2025

Published: 15 August 2025

**Citation:** Fazal, A.; Iqbal, M.J.; Raza, M.A.; Almutairi, B.S.; Zakaly, H.M.H.; Akhtar, N.; Irshad, M.; Riaz, S.

Exploring the Potential of Green Synthesized  $\text{Sr}_{0.8}\text{Ce}_{0.2}\text{Fe}_{0.8}\text{Co}_{0.2}\text{O}_3$  Using Orange and Lemon Extracts for Hybrid Supercapacitor Applications.

*Batteries* **2025**, *11*, 310. <https://doi.org/10.3390/batteries11080310>

**Copyright:** © 2025 by the authors. Licensee MDPI, Basel, Switzerland. This article is an open access article distributed under the terms and conditions of the Creative Commons Attribution (CC BY) license (<https://creativecommons.org/licenses/by/4.0/>).

## 1. Introduction

For a clean, energy-efficient system, shifting to renewable natural resources is necessary. These include solar energy, wind energy, etc., but the drawback of utilizing these resources is their discontinuous supply [1,2]. To resolve this issue, the scientific community is striving hard to manufacture energy storage devices with high capacity, cyclic life, energy and power density [3–6]. Supercapacitors are emerging energy storage devices that can provide all the above-mentioned advantages. They mainly consist of electrical double-layer capacitors (EDLCs) and pseudocapacitors. The working principle of EDLCs involves adsorption and desorption of ions which results in high cyclic stability [7–10]. On the other

hand, pseudocapacitors work through redox reactions and result in high specific capacitance values. The combination of the two types results in asymmetric hybrid supercapacitor devices that have high specific capacitance as well as good cyclic stability [11,12].

Pseudocapacitors are mainly tested as positive electrodes and are further categorized into three types. The first type is redox potential, which stores charge through metal electrode polarization that occurs below the redox potential of the electrode material. The second is redox pseudocapacitance, which undergoes surface redox reactions. In surface redox reactions, the electrolyte ions accumulate near the electrode surface, and the exchange of electrolyte ions and electrons occurs, which is responsible for charge storage. Examples are metal oxides and conducting polymers. The third type is intercalation pseudocapacitors in which the ions intercalate into the electrode material. The phenomenon of intercalation and de-intercalation makes them high-energy storage devices [13]. The materials that fall under the category of intercalation pseudocapacitors are some metal-oxides, conducting polymers and new emerging perovskite oxides [14–17]. Perovskites are intercalation pseudocapacitive materials that are gaining popularity due to low cost, high-energy density and high oxygen vacancies [18].

The general formula for perovskite oxides is  $\text{ABO}_3$ , where A denotes alkali or rare earth metals (La, Sr, Ce) and B denotes transition metals (Co, Fe, Mn). A site element takes up the centre of eight octahedra and is responsible for thermodynamic stability. In contrast, the B site element forms an octahedral with six oxygen atoms and undergoes electrochemical reactions [19–22]. They are rich in oxygen vacancies, which are responsible for their metallic character. The high electrical conductivity arises from the crossover of the Fermi level between the 3d orbital of the B-site element and the 2p orbital of oxygen in terms of the density of states. They work on the mechanism of oxygen ion  $\text{O}^{2-}$  intercalation. The advantage of  $\text{O}^{2-}$  intercalation over  $\text{Li}^+$  and  $\text{Na}^+$  is that it can accommodate two charges, which means that double the number of charges can be stored in a single charge-discharge cycle compared to monovalent  $\text{Li}^+$  and  $\text{Na}^+$ . Since they undergo oxygen intercalation, it is essential to synthesize perovskite material with high oxygen vacancies for improved electrochemical performance [23].

Among all the perovskites, strontium-based materials have received considerable attention due to their natural abundance, high conductivity and cost-effectiveness [24–27]. Various strontium-based perovskites have been reported in the literature, particularly strontium ferrites [28–30]. According to the literature, appropriate element doping in these perovskites can induce structure distortion that is responsible for creating oxygen vacancies. Cerium is considered a good choice for A-site doping as it increases defect sites and has multiple oxidation states,  $\text{Ce}^{+3}$  and  $\text{Ce}^{+4}$ , required for enhanced oxygen diffusion [31,32]. Moreover, aliovalent doping at the A-site generates redox couple  $\text{B}^{n+}/\text{B}^{(n+1)+}$ , which enhances electrochemical performance.

The synthesis technique is an important parameter because the morphology and crystal structure of the material depend on it. There are various synthesis parameters to synthesize perovskite, such as ball milling, co-precipitation, the auto-combustion method, etc. The ball milling method involves heating the material at a high temperature that renders it with sluggish surface area properties. Co-precipitation involves low temperature, which results in non-uniform and agglomerated particles. The auto-combustion method is desirable for synthesizing perovskite material as it results in a controlled structure, uniform particle distribution and porosity, due to the evolution of gases that occur during combustion reactions. The disadvantage of the auto-combustion method is using non-biocompatible fuel as a chelating/reducing agent. The literature has reported that fuel plays a significant role as the material's morphology, porosity and surface area depend on it. To create a bio-compatible system, the reactants and by-products should be non-toxic,

eco-friendly, cost-effective, and easy to handle [33]. Many studies have discussed the role of different chelating agents and concluded that they affect the morphology and crystallite size of the material [34,35]. Green synthesis can provide an alternative to toxic chemicals by using biocompatible reducing agents.

Herein, we have used bio-compatible green reducing agents, i.e., ORJ and LMJ, to synthesize the perovskite material  $\text{Sr}_{0.8}\text{Ce}_{0.2}\text{Fe}_{0.8}\text{Co}_{0.2}\text{O}_3$  using the green auto-combustion method. Strontium-based perovskite is utilized because it is extensively studied in the literature and would make it easier to compare the results of bio-compatible chelating agents with non-biocompatible chelating agents. Furthermore, the cerium is used as an A-site substitution to stabilize the perovskite structure, and cobalt at the B-site is used because of its intrinsically high electronic and ionic conductivity. Two different fuels are used to study how the evolution of gases affects the reaction kinetics and results in different morphologies and crystallite sizes. The aim is to determine the effect of using a biocompatible reducing agent on the electrochemical performance of both electrodes. To the best of our knowledge, there is no previous work on synthesizing perovskite using plant extract and using it for supercapacitor application. This work will pave the way for using biocompatible reducing agents to synthesize perovskite material and exploit it in supercapacitor applications.

## 2. Materials and Methods

### 2.1. Powder Synthesis

All the materials were purchased from Sigma Aldrich and were used without further purification. Double-distilled water was obtained from the Milli-Q system. For the green auto-combustion synthesis method, lemon and orange juices were used as reducing agents. They were procured from the local market. To extract the lemons and oranges, they were first washed with DI water to remove any impurities. Then, with the help of a squeezer, their juice was extracted. The juice was filtered through Whatman filter paper various times to remove any residuals. The synthesis started by mixing the stoichiometric amount of strontium nitrate ( $\text{Sr}(\text{NO}_3)_2$ ), cerium nitrate hexahydrate ( $\text{Ce}(\text{NO}_3)_3 \cdot 6\text{H}_2\text{O}$ ), iron nitrate nanohydrate ( $\text{Fe}(\text{NO}_3)_3 \cdot 9\text{H}_2\text{O}$ ) and cobalt nitrate hexahydrate ( $\text{Co}(\text{NO}_3)_2 \cdot 6\text{H}_2\text{O}$ ) in 20 mL of double-distilled water, individually. After that, the individual solutions were added to one large beaker. The stirring and heating were performed until a homogeneous solution was obtained. Then, 20 mL of lemon juice/orange juice was added dropwise as a fuel/reducing agent and left on the hot plate at 80 °C until the solution turned into a gel. The gel was then converted into ash after auto-combustion occurred. The ash was ground into powder, calcinated at 600 °C for 4 h, and then sintered at 1100 °C for 2 h. The whole synthesis process is schematically depicted in Figure 1.

### 2.2. Electrode Fabrication

After powder synthesis, electrodes were fabricated using the slurry method. Nickel (Ni) foam was used as the current collector and washed with 3 M HCl, ethanol, and DI water. The synthesized perovskite, carbon black and PVDF were dissolved in DMF solvent in a ratio of 80:10:10. The slurry was subjected to magnetic stirring until homogenously dispersed and then coated on pre-washed Ni foam (1 cm<sup>2</sup> area). After coating, the electrodes were dried in an oven at 80 °C. The mass of the slurry on the electrodes was ~6 mg/cm<sup>2</sup>. The electrode in which the active material is synthesized from an orange juice-reducing agent is termed ORJ, and the other one as LMJ.

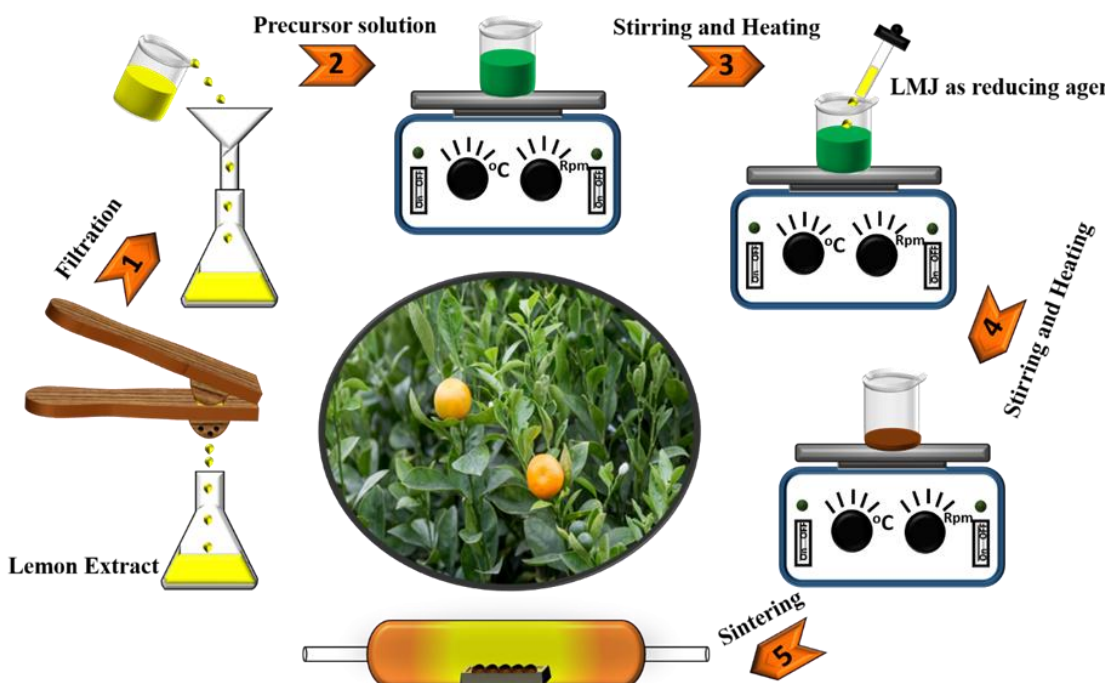


**Figure 1.** Schematic diagram of material synthesis.

### 2.3. Powder Characterization

The powder was characterized using X-ray Diffraction (XRD), Scanning Electron Microscopy (SEM), Energy Dispersive X-ray (EDX), Fourier Transform Infrared Spectroscopy (FTIR) and Photoluminescence (PL). XRD pattern was obtained from diffractogram (Equinox 2000, Thermo Scientific, Waltham, MA, USA) for the  $20^\circ$ – $80^\circ$  theta range. SEM (Inspect S50, Thermo Scientific, Waltham, MA, USA) and EDAX (EDAX, Mahwa, NJ, USA) were used to study the material's morphology and elements' quantitative analysis. FTIR (Thermo Scientific Nicolet IS5 Instrument, Waltham, MA, USA) was performed for functional group analysis. For photoluminescence (FS5, Edinburgh Instruments, Livingston, UK) spectra, spectrofluorometer was used.

### 2.4. Electrochemical Characterization

The electrochemical performance of the electrodes LMJ and ORJ was first carried out in a three-electrode assembly. In a three-electrode assembly, LMJ and ORJ were used as working electrodes, Hg/HgO as the reference electrode and a graphite rod as the counter electrode. The device of the best electrode was then fabricated with LMJ as the positive electrode and activated carbon (AC) as the negative electrode. The filter paper was sandwiched between the two electrodes that acted as a separator, saving the device from a short-circuit. Throughout the experiment, 1 M aqueous electrolyte (KOH) was used. All the electrochemical characterization is carried out using Potentiostat 3000 (Gamry, Warminster, PA, USA). The charge was balanced for the device using the following equations [36,37]:

$$\frac{m_{LMJ}}{m_{AC}} = \frac{C_s_{AC} \times \Delta V P_{AC}}{C_s_{LMJ} \times \Delta V P_{LMJ}} \quad (1)$$

where  $m$  denotes the mass,  $C_s$  denotes the specific capacity obtained in a three-electrode assembly and  $\Delta V$  denotes the potential window of the respective electrodes.

The specific capacity values obtained from CV and GCD, respectively, using the following formula [38]:

$$C_s = \frac{\int I(v)dt}{v \times m} \quad (2)$$

where  $\int I(v)dt$  is the area under the positive curve,  $v$  scan rate.

$$C_s = \frac{2 \times \int I(v)dt}{m \times \Delta V} \quad (3)$$

where  $\int Vdt$  is the area under the discharge curve and  $\Delta V$  is the potential window.

Energy density and power density are calculated by using the following formula:

$$\text{Energy Density}(E_d) = \frac{Cs \times \Delta V^2}{2 \times 3.6} \quad (4)$$

$$\text{Power Density}(P_d) = \frac{3600 \times E_d}{\Delta t} \quad (5)$$

where  $\Delta t$  is discharge time [39,40].

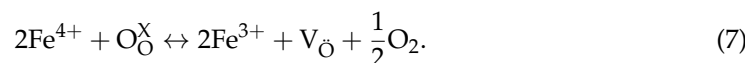
### 3. Results and Discussion

#### 3.1. Crystal Structure

The crystal structure and phase of the as-synthesized perovskite  $\text{Sr}_{0.8}\text{Ce}_{0.2}\text{Fe}_{0.8}\text{Co}_{0.2}\text{O}_3$  are analyzed by XRD pattern. The XRD pattern with the indexed peaks shown in Figure 2a matches the previously reported literature [28,41,42]. The perovskite has a cubic structure with space group Pm-3m. The cerium is said to stabilize the overall perovskite structure at about 15 mol% [43–45]. However, one peak of  $\text{Fe}_2\text{O}_3$  was also detected for both the reducing agents, which is matched with the COD database entry number (96-153-2122). This segregation could be due to the addition of cerium above 15 mol% to stabilize the cubic structure. No cobalt phase segregation is seen, which means cobalt is substituted easily at the B-site. The Rietveld refinement was carried out to extract the important structural information. It is given in Figure 2d,e for ORJ and LMJ. The LMJ refinement is done for both the phases of perovskite and  $\text{Fe}_2\text{O}_3$ . For ORJ, the  $\text{Fe}_2\text{O}_3$  peak is small and close to the noise data, due to which it was difficult to refine. The R-factors and chi ( $\chi$ ) value, are given in Table 1. Firstly, the tolerance factor is calculated to prove the cubic structure of the prepared perovskite. For this, the radius values are obtained from the refinement which are 2.15 Å, 1.82 Å, 1.26 Å, 1.25 Å and 0.74 Å for Sr, Ce, Fe, Co and O, respectively. The formula for tolerance factor is given below:

$$t = \frac{r_A + r_O}{r_B + r_O} \quad (6)$$

where  $r_A$ ,  $r_B$  and  $r_C$  are the radii of A-site, B-site cation and O anion, respectively [46]. The calculated tolerance factor for both ORJ and LMJ is calculated as 0.998, denoting a nearly cubic structure which is in accordance with our hypothesis and the literature. In order to maintain the cubic structure and charge neutrality of perovskite, the iron changes its oxidation state as follows [47]:



The greater ionic radii of  $\text{Fe}^{3+}$  led to the creation of oxygen vacancies desirable for improved electrochemical performance. The bond valence (BV) calculation is performed to obtain the oxidation state of both strontium and iron from the bond angle values using the following formula:

$$\text{BV} = \exp\left(\frac{R_o - R}{B}\right) \quad (8)$$

where  $R_0$  is the empirically derived bond valence,  $R$  is observed, and  $b$  is 0.37 as a universal constant.

$$\text{BVS} = \text{BV} * \text{CN} \quad (9)$$

where CN is the coordination number [48]. The bond valence sum (BVS) value gives the oxidation state of the element. The calculated values for both the LMJ and ORJ are given in Table 1.

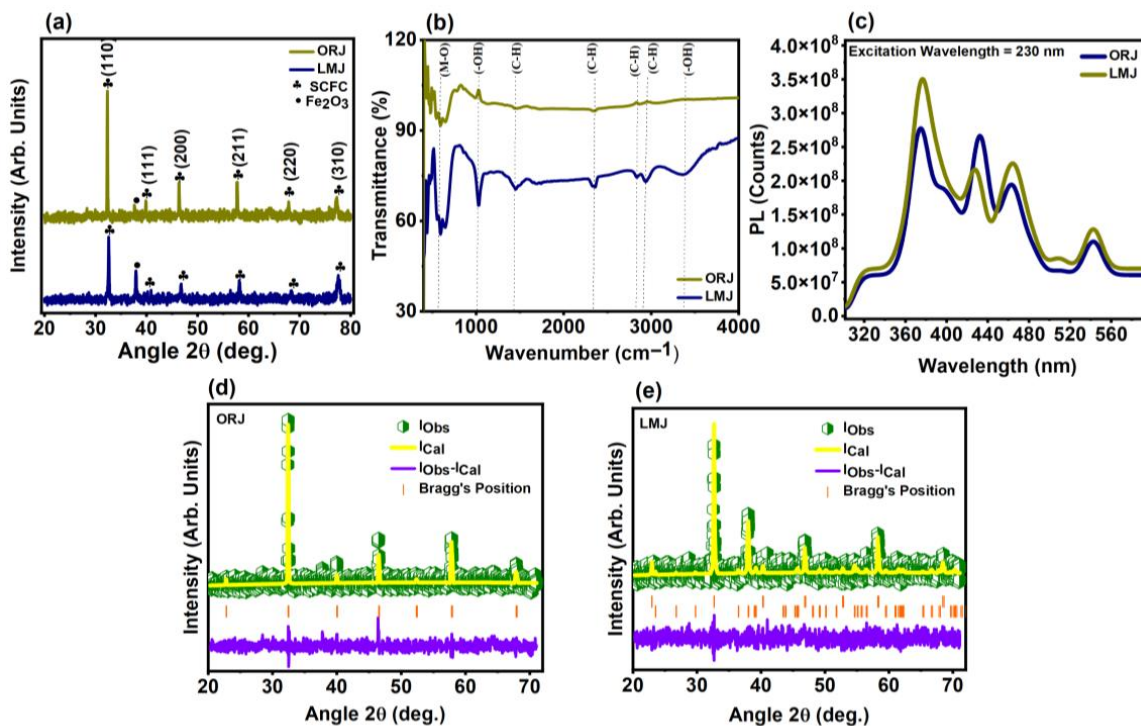


**Figure 2.** (a) XRD, (b) FTIR and (c) PL spectra of both ORJ and LMJ. XRD refinement of (d) ORJ with a single perovskite phase and (e) LMJ with both the perovskite and  $\text{Fe}_2\text{O}_3$  phase.

**Table 1.** Parameters obtained from Rietveld refinement.

Material	R-Factors			$\chi$	R	CN	BVS
	R <sub>p</sub>	R <sub>wp</sub>	R <sub>exp</sub>				
ORJ	Sr-O	12.5	15.7	1.27	2.76	12	2.12
	Fe-O				1.95	6	3.56
LMJ	Sr-O	13.3	16.7	1.18	2.74	12	2.20
	Fe-O				1.94	6	3.70

It can be seen that both LMJ and ORJ have Sr oxidation states close to +2, which means that strontium did not undergo oxidation state change. For Fe, ORJ has oxidation state +3.56 and LMJ +3.70, indicating the presence of  $\text{Fe}^{3+}$  and hence increased oxygen vacancies in both the materials. The crystallite size of the perovskite prepared from different fuels is calculated from the Scherrer formula:

$$\text{Crystallite size}(D) = \frac{k\lambda}{\beta \cos\theta} \quad (10)$$

where  $k$  is referred to as the shape factor,  $\lambda$  is the X-ray wavelength,  $\beta$  is the full-width at half maxima and  $\cos\theta$  is the angle at which the individual peaks appear [49,50]. Perovskite prepared from LMJ as a reducing agent has a lower crystallite size (36 nm) than ORJ (53

nm), which means it should possess a high surface area. The change in crystallite size calculated from XRD confirms how the combustion reaction with different reducing agents affects the material parameters.

### 3.2. Chemical Bond Analysis

FTIR is used to analyze the chemical composition of the material. Perovskites have the formula  $\text{ABO}_3$ , where A is located at the centre and B at the octahedral site surrounded by a coordination of six oxygen anions. The FTIR analysis for ORJ and LMJ was carried out for  $400\text{--}4000\text{ cm}^{-1}$ , as shown in Figure 2b. For perovskite, an intense peak appears around  $\sim 600\text{ cm}^{-1}$ , resulting in M–O bond stretching, where M is a transition metal [51]. For ORJ and LMJ, peaks appear at this wavelength supporting the XRD results of the successful synthesis of the perovskite structure. It can be seen that small peaks appear at  $1433\text{ cm}^{-1}$ ,  $2352\text{ cm}^{-1}$ ,  $2885\text{ cm}^{-1}$  and  $2944\text{ cm}^{-1}$ . These peaks are due to the symmetric and asymmetric stretching of C–H bonds. The peak around  $1000$  and  $3400\text{ cm}^{-1}$  in LMJ is due to the -OH group arising from the adsorption of water molecules on the surface [52].

### 3.3. Photoluminescence

Photoluminescence (PL) is used to study the optical and electronic properties of the material with respect to the defect states. Figure 2c shows the PL spectra of the obtained perovskite materials LMJ and ORJ. The PL spectra have prominent peaks at  $377$ ,  $431$ ,  $465$  and  $542\text{ nm}$ . The  $377\text{ nm}$  peak appears due to near-band emission. The peak appearing at  $377\text{ nm}$  is due to the recombination of electrons with structural defects [53]. ORJ has greater intensity for these defects, which means it has greater electron recombination, resulting in lower electrical conductivity. The oxygen vacancy-related defects appear around  $550\text{ nm}$  [54]. It can be seen in the figure that LMJ has greater oxygen vacancies than ORJ, as it has the highest intensity, which corroborates with XRD analysis. These oxygen vacancies provide sites for oxygen intercalation. Both factors increase the overall electrochemical performance of the LMJ electrode.

### 3.4. Morphological Study

The morphology and elemental composition are studied by SEM and EDX, respectively. The morphology of both ORJ and LMJ consists of irregularly shaped particles with varying sizes, as shown in Figure 3a,b,d,e. The particle size of LMJ is smaller than ORJ, as seen in SEM images. The smaller particle size of LMJ compared to ORJ depicts its high surface area, which is corroborated by the crystallite size of XRD. Hence, it can exhibit good electrochemical properties as compared to ORJ. The point analysis for element detection through EDX spectra is shown in Figure 3c,f. The presence of all the elements in LMJ and ORJ confirms their successful synthesis.

### 3.5. Electrochemical Performance in Three-Electrode Assembly

The electrochemical potential of the electrodes ORJ and LMJ is first analyzed in a three-electrode assembly before being utilized as a hybrid supercapacitor device. The cyclic voltammetry (CV) curves are plotted with potential (V vs. Hg/HgO) on the  $x$ -axis and current density on the  $y$ -axis. Both electrodes showed oxidation and reduction peaks, which means both were undergoing diffusion-controlled processes, confirming intercalation pseudocapacitance. Figure 4a,b shows the CV curves of both the ORJ and LMJ electrodes at various scan rates. As the electrodes show a diffusive-controlled mechanism, specific capacity is calculated and plotted as a scan rate function in Figure 4c. It can be seen that the specific capacity value is maximum at lower scan rates and decreases as we go up to the higher scan rates. This trend is due to insufficient time available for the diffusion of ions as

the scan rate increases. The highest specific capacity of 320 C/g is achieved for LMJ at a 1 mV/s scan rate, almost double that of ORJ, which is 160 C/g.

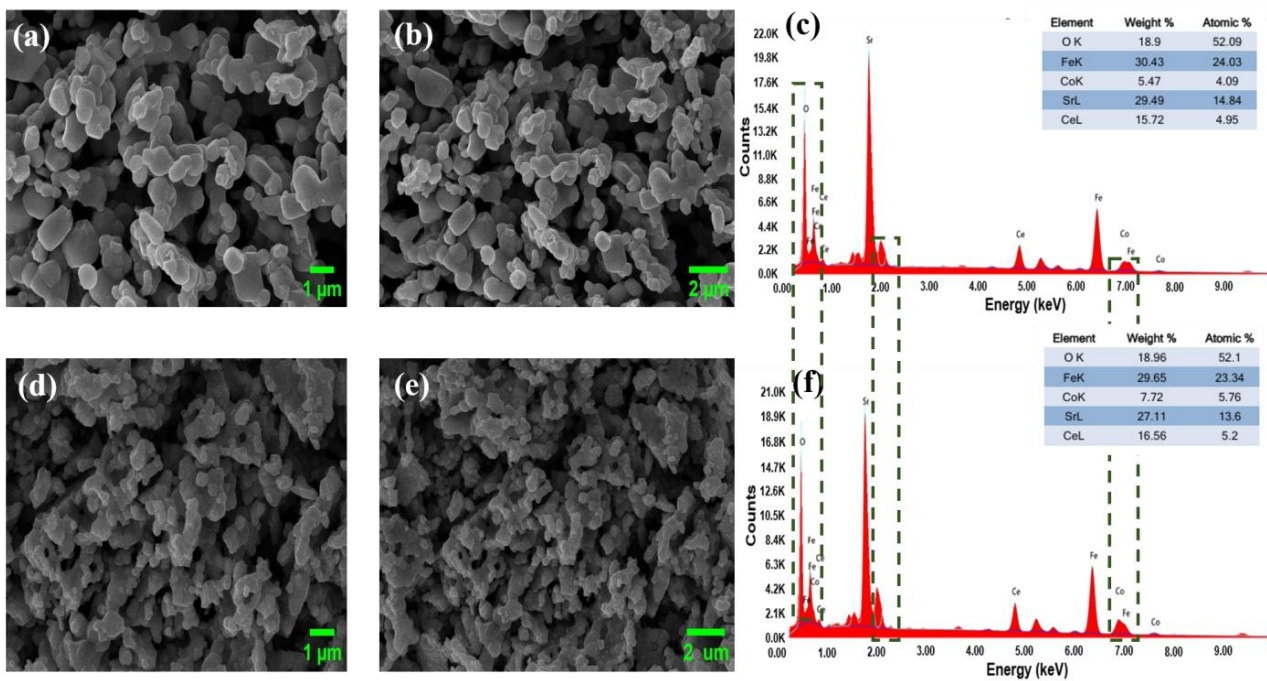


**Figure 3.** Morphological images of perovskite (a,b) ORJ and (d,e) LMJ showing irregularly shaped connected particles. The elemental analysis of (c) ORJ and (f) LMJ confirms the presence of all the elements.

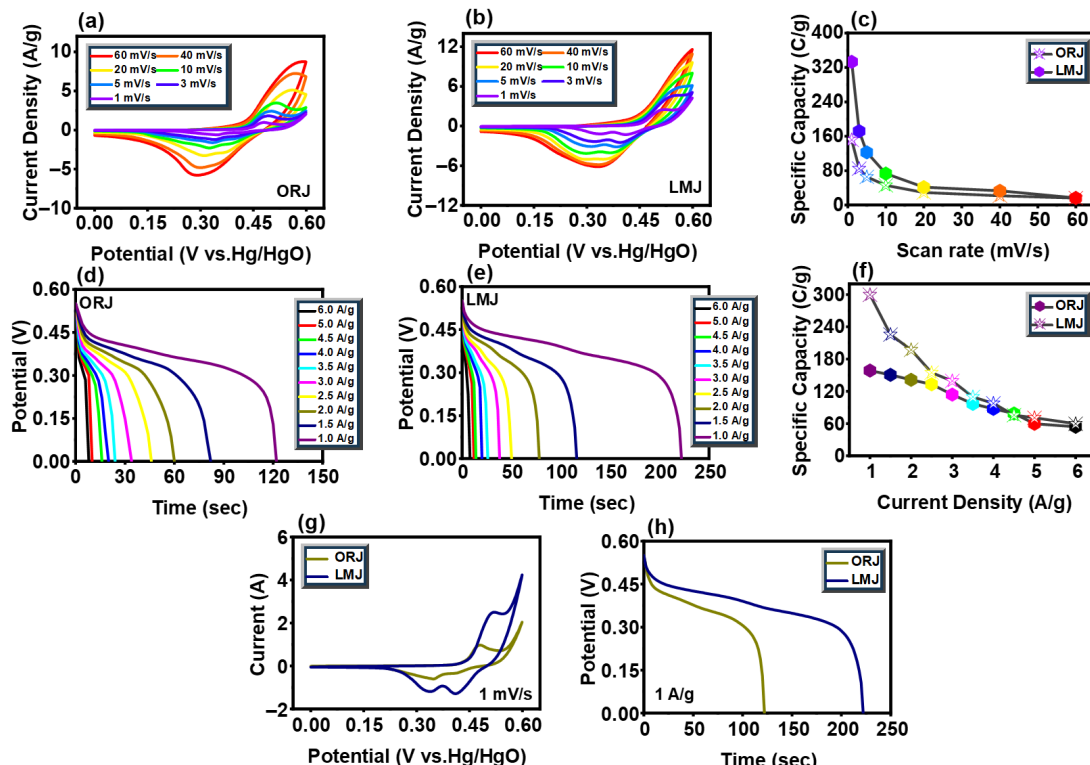


**Figure 4.** CV curves of (a) ORJ and (b) LMJ measured at different scan rates. (c) The specific capacity values are expressed as a function of the scan rate for both electrodes. GCD curves of (d) ORJ and (e) LMJ measured at different current densities. (f) The specific capacity values are expressed as a function of the current density for both electrodes. (g) CV comparison curve of LMJ and ORJ at 1 mV/s scan rate. (h) GCD comparison curve of LMJ and ORJ at 1 A/g current density.

Galvanostatic charge–discharge (GCD) was carried out for further electrochemical analysis. The discharge curves of ORJ and LMJ are plotted with potential on the *y*-axis and discharge time on the *x*-axis, as shown in Figure 4d,e. The plateaus in the discharge curves of both electrodes confirm the occurrence of diffusion-controlled mechanisms. The curves are taken at different current densities, and the calculated specific capacities as a function of these densities are shown in Figure 4f. The results correlate with the CV as LMJ has a high specific capacity of 300 C/g at 1 A/g current density compared to ORJ, which is only 158 C/g. Figure 4g shows comparison curves of both electrodes at a 1 mV/s scan rate, clearly showing the oxidation and reduction peaks for both electrodes, with LMJ having a greater area under the curve. Similarly, Figure 4h shows the discharge curve comparison with LMJ, showing a greater area than ORJ.

Cyclic stability and coulombic efficiency for the best-performing sample LMJ were calculated for 2500 cycles as shown in Figure 5a. Cyclic stability showed a decline at the start due to volume changes happening in perovskite, but after a few cycles, it was stabilized to 72%. However, the coulombic efficiency was retained at 98%. Electrochemical Impedance Spectroscopy (EIS) gives valuable electrochemical information on the electrode kinetics. Two plots are obtained from EIS at a frequency range of 0.1 Hz to 100 kHz: the Nyquist plot and the Bode plot. A comparison of the Nyquist plot is shown in Figure 5b. The starting region where the semi-circle forms is the high-frequency region, and the tail region is the low-frequency region. The two important parameters, namely electrical series resistance (ESR) and charge transfer resistance ( $R_{ct}$ ), are obtained from this plot. ESR depicts the ionic conductivity of the electrode, and the lower value denotes the material's good ionic conductivity.  $R_{ct}$  is charge transfer resistance, and its low value denotes the excellent interaction of electrolyte ions with the electrode material. ESR values for ORJ and LMJ are calculated as  $1.54\ \Omega$  and  $1.52\ \Omega$ .

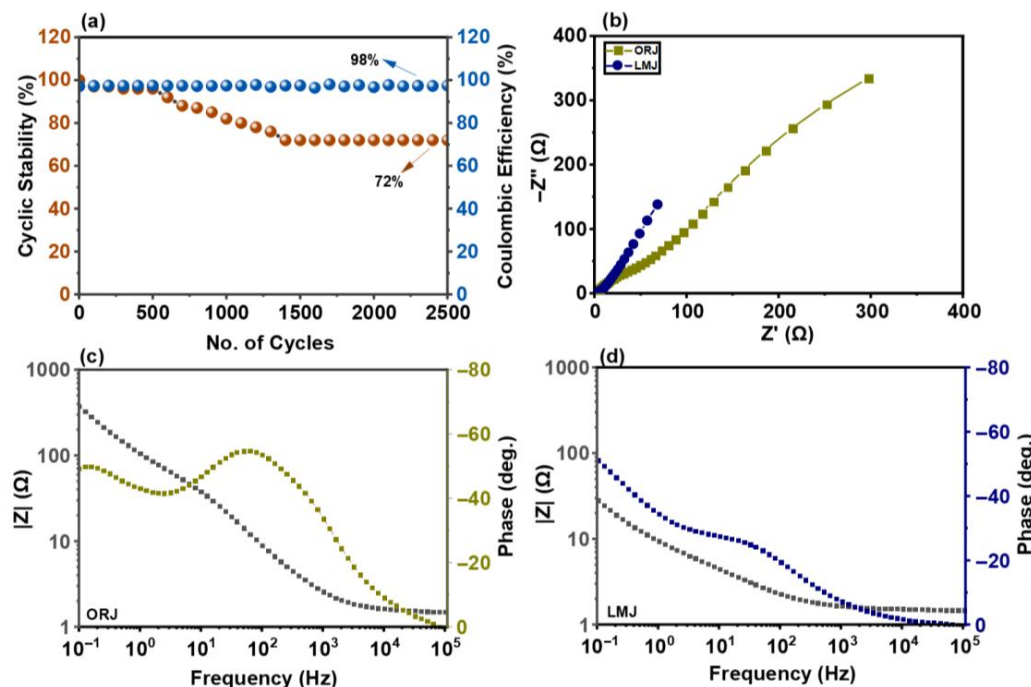


**Figure 5.** (a) Cyclic stability of LMJ for 2500 GCD cycles. (b) The Nyquist graph obtained from EIS is plotted between real impedance on the *x*-axis and imaginary impedance on the *y*-axis for both electrodes. The Bode plot for (c) LMJ and (d) ORJ shows a plot of impedance and phase angle as a function of frequency.

On the other hand, the  $R_{ct}$  value for LMJ is negligible as no significant semi-circle region is seen, whereas  $21.46\ \Omega$  was calculated for ORJ. The results showed that LMJ has good ionic conductivity and interaction with electrolyte ions. Figure 5c,d shows the Bode plot for LMJ and ORJ, respectively. It can be seen that LMJ has a lower impedance than ORJ, which is responsible for its good electrochemical performance. The phase angle close to  $90^\circ$  shows the capacitive behaviour of the electrode, whereas the deviation from  $90^\circ$  denotes the presence of redox reactions and a diffusive-controlled mechanism. Both electrodes show a deviation from  $90^\circ$ , further supporting their diffusive nature and the occurrence of redox reactions.

For the in-depth study of the mechanism, the b-value is calculated for both electrodes from the power law [55]. If the b-value is  $0.5 \geq b$ , the diffusive-controlled mechanism prevails,  $b \geq 1$ , the capacitive-controlled mechanism prevails and value  $1 > b \geq 0.5$  denotes the transition. Both electrodes have a b-value close to 0.5, as shown in Figure 6a. Hence, the diffusive-controlled mechanism prevails in both electrodes. To further dig into the charge contribution, the Trasatti method is used, which quantifies the inner charge contribution and outer charge distribution [56]. The intercepts of the plots in Figure 6c,e are used to calculate the inner charge contribution for ORJ and LMJ, respectively. Likewise, the intercepts of the plot in Figure 6d,f are used to calculate the inner charge contribution for ORJ and LMJ, respectively. The ORJ showed 4% outer and 96% inner charge storage, while the LMJ showed 6% outer and 93% inner charge storage. Figure 6g,h shows the  $R^2$  values for ORJ and LMJ, respectively.  $R^2$  values closer to 1 show good reversibility of reactions, and both electrodes have values closer to 1.

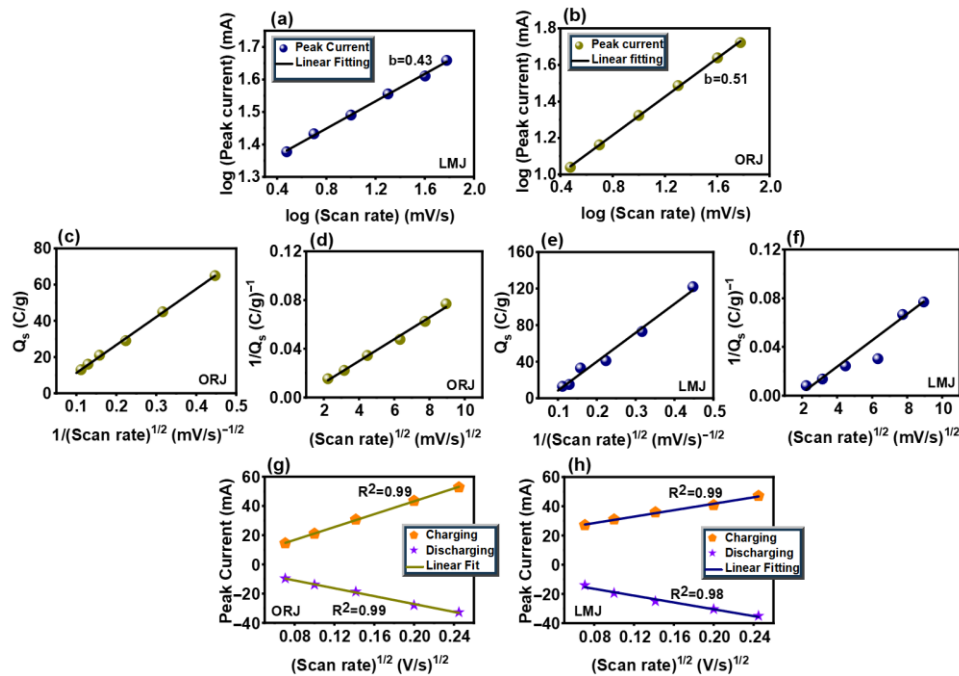


**Figure 6.** (a,b) b-value calculation for LMJ and ORJ, respectively, from the graph plotted between log peak current versus log scan rate. Outer and inner charge calculation for (c,d) ORJ and (e,f) LMJ using the Trasatti Method. (g,h)  $R^2$  value graph for the fabricated electrodes to check the reversibility of the electrode.

The capacitive and diffusive contribution at each scan rate is calculated by Dunn's model, which is given as follows [57]:

$$i(V) = k_1 v + k_2 v^{1/2}. \quad (11)$$

By rearranging the equation, it becomes:

$$\frac{i(V)}{v^{1/2}} = k_1 v + k_2 \quad (12)$$

where  $k_1$  is slope and  $k_2$  is intercept. Figure 7a,b is plotted between potential and current density for ORJ and LMJ, respectively, at a 5 mV/s scan rate. The purpose of this is to identify the capacitive contribution from the CV data obtained experimentally. It can be clearly seen that LMJ has a more diffusive area. The capacitive and diffusive contribution at each scan rate is depicted in Figure 7c,d. At low scan rates, the diffusive mechanism is dominant, and at higher scan rates, the capacitive mechanism dominates. For the LMJ electrode, the diffusive mechanism dominates at each scan rate as compared to ORJ because of high oxygen ion intercalation. To confirm this, the diffusion coefficient is calculated using the following equation:

$$D = \frac{R^2 T^2}{2 A^2 n^4 F^4 C^2 \sigma^2} \quad (13)$$

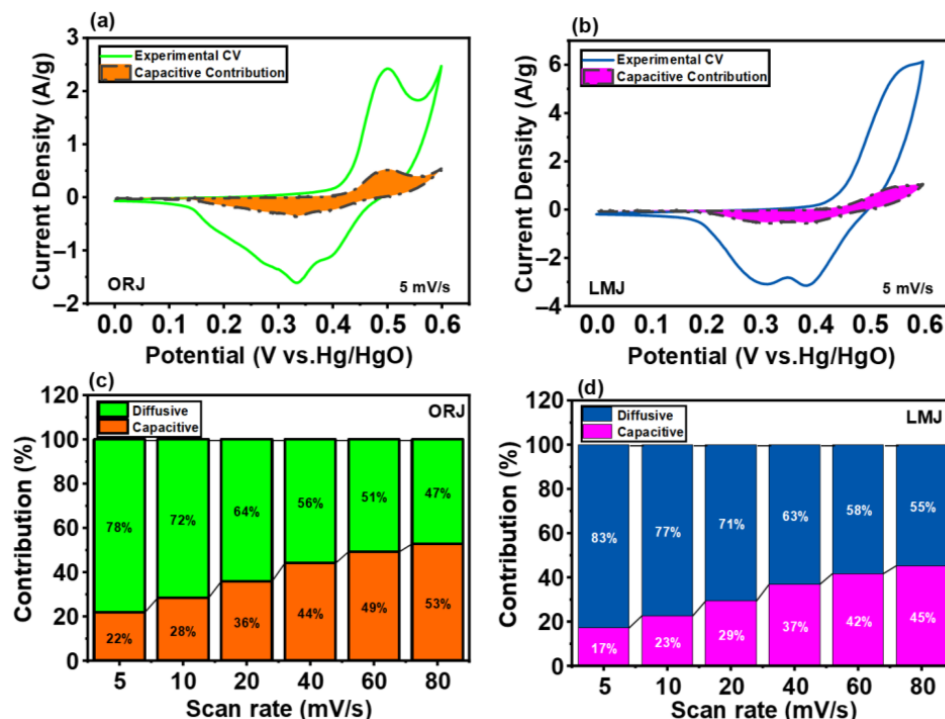


**Figure 7.** The figure shows the capacitive contribution part from experimental CV data at a 5 mV/s scan rate for (a) ORJ and (b) LMJ. Capacitive and diffusive contributions at each scan rate for (c) ORJ and (d) LMJ.

In the above equation,  $D$  is the diffusion coefficient,  $R$  is the universal gas constant ( $8.314 \text{ J mol}^{-1} \text{ K}^{-1}$ ),  $T$  is temperature in kelvin,  $A$  is surface area in  $\text{cm}^2$ ,  $n$  is the number of electrons transfer,  $F$  is Faraday's constant ( $96485 \text{ C mol}^{-1}$ ),  $C$  is the molar concentration of ions in  $\text{mol cm}^{-3}$  and  $\sigma$  is the Warburg co-efficient. The Warburg coefficient is obtained from the slope of  $Z'$  versus  $\omega^{-1/2}$  [58]. The diffusion coefficient calculated from Equation (13) is  $5.58 \times 10^{-12}$  for LMJ and  $7.59 \times 10^{-14}$  for ORJ. Hence, the results correlate with the high diffusive contribution of LMJ as it has a high oxygen diffusion coefficient.

### Working Mechanism

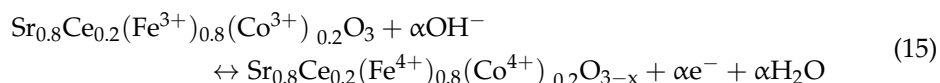
The LMJ and ORJ work on the oxygen anion-type intercalation charge storage mechanism. The structure obtained from Vesta software (Version 4.0.0) after refinement is shown in Figure 8. The addition of cerium led to the formation of oxygen vacancies as discussed

above and provides an increased number of active sites for oxygen intercalation. On the other hand, cobalt has good ionic conductivity that facilitates enhanced diffusion of ions. First, the  $\text{OH}^-$  ion from the electrolyte reaches the electrode surface, where it undergoes the dissociation process as follows:

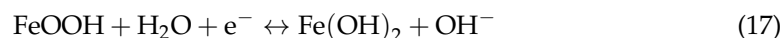
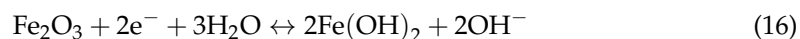


This  $\text{O}^{2-}$  ion will diffuse across the perovskite grain boundaries and reach the oxygen vacancies present. As a result of the intercalation of this oxygen anion, the transition metal oxides will change their oxidation states [28] according to Equation (15):

### Oxygen Intercalation



### Surface Redox Pseudocapacitance



Due to the presence of segregated  $\text{Fe}_2\text{O}_3$ , it contributed to surface pseudocapacitance as shown in Equations (16) and (17) [59]. The electrochemical performance in the three-electrode assembly concluded that the LMJ was a better-performing electrode than ORJ because of the advantage of small particle size, which endowed it with good electrical conductivity. Secondly, the greater phase segregation of the secondary phase in LMJ contributed to enhanced surface pseudocapacitance along with oxygen intercalation.

The results are also comparable with the reported literature for similar perovskite materials in Table 2.

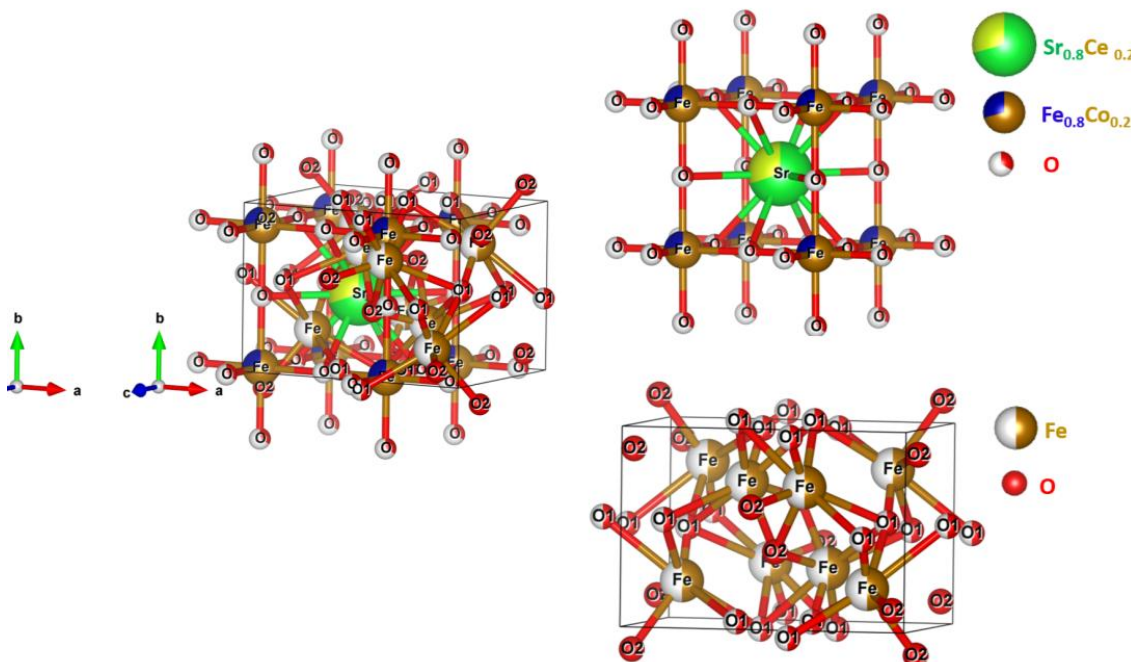


**Figure 8.** The schematic diagram shows the mixed-phase  $\text{Sr}_{0.8}\text{Ce}_{0.2}\text{Fe}_{0.8}\text{Co}_{0.2}\text{O}_3$  perovskite and  $\text{Fe}_2\text{O}_3$  structure.

**Table 2.** Comparison of synthesized  $\text{Sr}_{0.8}\text{Ce}_{0.2}\text{Fe}_{0.8}\text{Co}_{0.2}\text{O}_3$  with the reported literature.

Sr. No	Material	Synthesis Method	Electrolyte	Capacity	Capacitance	Ref.
1	$\text{SrCo}_{0.5}\text{Fe}_{0.5}\text{O}_3$	Sol-gel	1 M KOH	-	219 F/g at 2 A/g	[60]
2	$\text{SrFe}_{0.8}\text{Co}_{0.2}\text{O}_3$	Combustion Sol-gel	1 M KOH	-	433 F/g at 2 A/g	[28]
3	$\text{SrCo}_{0.9}\text{Fe}_{0.1}\text{O}_{3-\delta}$	Solid-state Reaction	1 M NaOH	-	526 F/g at 1 A/g	[61]
4	$\text{La}_{0.7}\text{Sr}_{0.3}\text{Mn}_{0.5}\text{Fe}_{0.5}\text{O}_3$	Sol-gel Auto-combustion	3 M KOH	330 C/g at 1 A/g	-	[62]
5	$\text{SrFe}_{0.85}\text{Zr}_{0.15}\text{O}_{3-\delta}$	Solid-state Reaction	2 M KOH	-	163 F/g at 0.5 A/g	[29]
6	$\text{Sr}_{0.8}\text{Ce}_{0.2}\text{Fe}_{0.8}\text{Co}_{0.2}\text{O}_3$ (ORJ), (LMJ)	Auto-combustion	1 M KOH	158 C/g, 300 C/g at 1 A/g	300 F/g, 544 F/g at 1 A/g	This work

### 3.6. Electrochemical Performance in Two-Electrode Assembly

The best-performing electrode, LMJ, was utilized in a hybrid supercapacitor device ( $\text{LMJ} \parallel \text{AC}$ ) with LMJ as the positive electrode and commercially available activated carbon (AC) as the negative electrode. The potential window of 1.6 V is selected based on the potential window of individual electrodes, as shown in Figure 9a. The device is operated at different scan rates to see the electrochemical behaviour, as shown in Figure 9b. It can be seen that the CV curves are quasi-rectangular with redox peaks that confirm both the capacitive (due to the activated carbon electrode) and diffusive (LMJ electrode) charge storage mechanisms occurring in the device. The curves maintain shape at low and high scan rates, showing electrochemical reversibility. Figure 9c shows the galvanostatic charge-discharge curves of the device at different current densities. The curves maintain triangular symmetry with slight plateaus, confirming the occurrence of both mechanisms. The specific capacity values are calculated and given as a function of current density in Figure 9d. The highest capacity achieved for the  $\text{LMJ} \parallel \text{AC}$  device is 364 C/g at 1 A/g current density, received due to the synergistic effect of both electrodes. Cyclic stability is essential to determine the practical application of the device. The excellent device showed 98% cyclic stability over 5000 GCD cycles. It not only demonstrated high cyclic stability of 98%, but also showed good coulombic efficiency of 99%, as shown in Figure 9e. The Nyquist plot before and after the cyclic stability test is shown in Figure 9f. The ESR value increased slightly from 2.2 to 2.4  $\Omega$  after 5000 GCD cycles. The  $R_{ct}$  value before the cyclic test was negligible, and after, it was 5 ohms, which could be due to the continuous intercalation and de-intercalation of ions.

The b-value is calculated to depict the charge storage mechanism, as seen in Figure 10a. For the device, the b-value closer to 0.5 depicts diffusive-controlled behaviour, the one closer to 1 represents the capacitive mechanism, and the values in between show the presence of both. The b-value calculated for the device is 0.75, showing that the device is a hybrid supercapacitor working on both mechanisms. The capacitive and diffusive contribution for the  $\text{LMJ} \parallel \text{AC}$  device at each scan rate is calculated by Dunn's model using Equation (12).

The diffusive-controlled mechanism dominates at lower scan rates, and the capacitive mechanism dominates at higher scan rates, as shown in Figure 10b. Energy and power density are crucial for the practical utilization of the device. Figure 10c shows the comparison of energy and power density of this work with the reported literature as a Ragone plot [29,63–67]. The highest energy density achieved is 80 Wh/kg at a power density of 3609 W/kg at 1 A/g current density, making it a well-performing device.

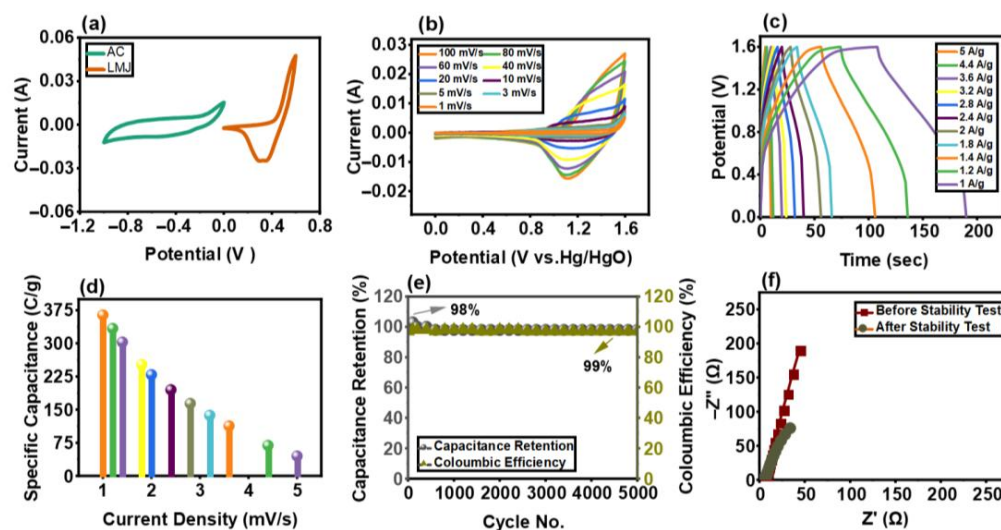


**Figure 9.** (a) CV curves of the positive (LMJ) and negative electrode (AC) to determine the working potential of the electrode. (b) CV and (c) GCD curves of the fabricated LMJ || AC device. (d) Specific capacity values are obtained at different current densities. (e) Capacitance retention and coulombic efficiency over 5000 cycles are expressed in the graph plot. (f) Nyquist plot obtained from EIS before and after 5000 GCD cycles.

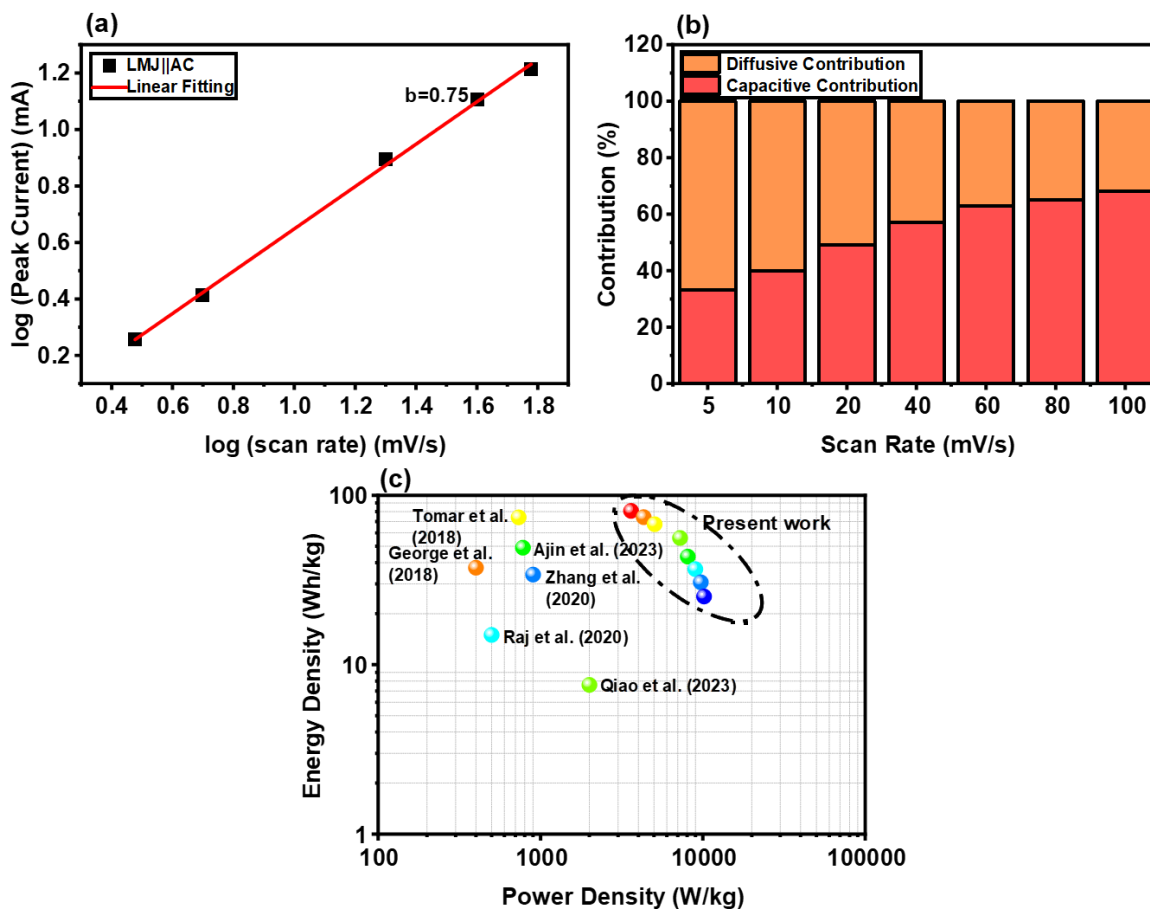


**Figure 10.** (a) The b-value calculation for the LMJ || AC device. (b) Capacitive and diffusive contribution percentages obtained at different scan rates. (c) Ragone plot of the device showing power density on the x-axis and energy density on the y-axis [29,63–67].

#### 4. Conclusions

In conclusion, the facile and simple auto-combustion method was used to synthesize the  $\text{Sr}_{0.8}\text{Ce}_{0.2}\text{Fe}_{0.8}\text{Co}_{0.2}\text{O}_3$  perovskite with two different bio-compatible reducing agents. The XRD confirmed the successful synthesis of perovskite with a cubic crystal structure for both reducing agents. The transition of  $\text{Fe}^{4+}$  to  $\text{Fe}^{3+}$  introduces oxygen vacancies, which is further confirmed by Rietveld refinement of XRD data and PL spectra. The abundant oxygen vacancies, larger surface area and secondary phase proved to be favourable for the electrochemical performance of LMJ. The fabricated LMJ || AC device showed a remarkable 98% cyclic stability even after 5000 GCD cycles. This study explores the effective utilization of bio-compatible reducing agents for synthesizing perovskites and utilizing them for supercapacitor device fabrication.

**Author Contributions:** A.F.: Conceptualization, Data Curation, Investigation, Methodology, Visualization, Writing—original draft. M.J.I.: Supervision, Conceptualization, Validation, Funding, Writing—review and editing. M.A.R.: Supervision, Validation, Writing—review and editing. B.S.A.: Formal Analysis, Funding, Writing—review and editing. H.M.H.Z.: Formal Analysis, Validation, Visualization. N.A.: Formal Analysis, Visualization, Validation. M.I.: Methodology, Visualization, Formal Analysis. S.R.: Validation, Visualization. All authors have read and agreed to the published version of the manuscript.

**Funding:** This research work was partially supported by the University of the Punjab, Lahore, Pakistan, through a research project grant for the fiscal year 2024–2025. In addition, this research was supported by Princess Nourah bint Abdulrahman University Researchers Supporting Project Number (PNURSP2025R327), Princess Nourah bint Abdulrehman University, Riyadh, Saudi Arabia.

**Data Availability Statement:** Data will be provided on demand.

**Acknowledgments:** The authors acknowledges the funding by Princess Nourah bint Abdulrehaman University Researchers Supporting Project Number (PNURSP2025R327), Princess Nourah bint Abdulrehman University, Riyadh, Saudi Arabia.

**Conflicts of Interest:** The authors declare no conflicts of interest.

#### References

1. Dhaouadi, R.; Al-Othman, A.; Aidan, A.A.; Tawalbeh, M.; Zannerni, R. A Characterization Study for the Properties of Dust Particles Collected on Photovoltaic (PV) Panels in Sharjah, United Arab Emirates. *Renew. Energy* **2021**, *171*, 133–140. [[CrossRef](#)]
2. Mahmoud, M.; Ramadan, M.; Olabi, A.-G.; Pullen, K.; Naher, S. A Review of Mechanical Energy Storage Systems Combined with Wind and Solar Applications. *Energy Convers. Manag.* **2020**, *210*, 112670. [[CrossRef](#)]
3. Jiang, H.; Ma, H.; Jin, Y.; Wang, L.; Gao, F.; Lu, Q. Hybrid  $\alpha\text{-Fe}_2\text{O}_3@\text{Ni(OH)}_2$  Nanosheet Composite for High-Rate-Performance Supercapacitor Electrode. *Sci. Rep.* **2016**, *6*, 31751. [[CrossRef](#)] [[PubMed](#)]
4. Samantaray, S.; Mohanty, D.; Hung, I.-M.; Moniruzzaman, M.; Satpathy, S.K. Unleashing Recent Electrolyte Materials for Next-Generation Supercapacitor Applications: A Comprehensive Review. *J. Energy Storage* **2023**, *72*, 108352. [[CrossRef](#)]
5. Du, N.; Zheng, W.; Li, X.; He, G.; Wang, L.; Shi, J. Nanosheet-Assembled NiS Hollow Structures with Double Shells and Controlled Shapes for High-Performance Supercapacitors. *Chem. Eng. J.* **2017**, *323*, 415–424. [[CrossRef](#)]
6. Zhou, Y.; Maleski, K.; Anasori, B.; Thostenson, J.O.; Pang, Y.; Feng, Y.; Zeng, K.; Parker, C.B.; Zauscher, S.; Gogotsi, Y.; et al.  $\text{Ti}_3\text{C}_2\text{T}_x$  MXene-Reduced Graphene Oxide Composite Electrodes for Stretchable Supercapacitors. *ACS Nano* **2020**, *14*, 3576–3586. [[CrossRef](#)]
7. Tatrari, G.; Karakoti, M.; Tewari, C.; Pandey, S.; Bohra, B.S.; Dandapat, A.; Sahoo, N.G. Solid Waste-Derived Carbon Nanomaterials for Supercapacitor Applications: A Recent Overview. *Mater. Adv.* **2021**, *2*, 1454–1484. [[CrossRef](#)]
8. Maity, C.K.; Goswami, N.; Verma, K.; Sahoo, S.; Nayak, G.C. A Facile Synthesis of Boron Nitride Supported Zinc Cobalt Sulfide Nano Hybrid as High-Performance Pseudocapacitive Electrode Material for Asymmetric Supercapacitors. *J. Energy Storage* **2020**, *32*, 101993. [[CrossRef](#)]
9. Oje, A.I.; Ogwu, A.A.; Mirzaeian, M.; Tsendlzughul, N.; Oje, A.M. Pseudo-Capacitance of Silver Oxide Thin Film Electrodes in Ionic Liquid for Electrochemical Energy Applications. *J. Sci. Adv. Mater. Devices* **2019**, *4*, 213–222. [[CrossRef](#)]
10. Li, X.; Wei, B. Supercapacitors Based on Nanostructured Carbon. *Nano Energy* **2013**, *2*, 159–173. [[CrossRef](#)]

11. Abbas, Q.; Raza, R.; Shabbir, I.; Olabi, A.G. Heteroatom Doped High Porosity Carbon Nanomaterials as Electrodes for Energy Storage in Electrochemical Capacitors: A Review. *J. Sci. Adv. Mater. Devices* **2019**, *4*, 341–352. [CrossRef]
12. Ponce, M.F.; Mamani, A.; Jerez, F.; Castilla, J.; Ramos, P.B.; Acosta, G.G.; Sardella, M.F.; Bavio, M.A. Activated Carbon from Olive Tree Pruning Residue for Symmetric Solid-State Supercapacitor. *Energy* **2022**, *260*, 125092. [CrossRef]
13. Augustyn, V.; Simon, P.; Dunn, B. Pseudocapacitive Oxide Materials for High-Rate Electrochemical Energy Storage. *Energy Environ. Sci.* **2014**, *7*, 1597–1614. [CrossRef]
14. Sahoo, R.; Pal, A.; Pal, T. Noble Metal–Transition Metal Oxides/Hydroxides: Desired Materials for Pseudocapacitor. In *Noble Metal–Metal Oxide Hybrid Nanoparticles*; Elsevier: Amsterdam, The Netherlands, 2019; pp. 395–430.
15. Brezesinski, K.; Wang, J.; Haetge, J.; Reitz, C.; Steinmueller, S.O.; Tolbert, S.H.; Smarsly, B.M.; Dunn, B.; Brezesinski, T. Pseudocapacitive Contributions to Charge Storage in Highly Ordered Mesoporous Group V Transition Metal Oxides with Iso-Oriented Layered Nanocrystalline Domains. *J. Am. Chem. Soc.* **2010**, *132*, 6982–6990. [CrossRef] [PubMed]
16. Umar, A.; Ahmed, F.; Ullah, N.; Ansari, S.A.; Hussain, S.; Ibrahim, A.A.; Qasem, H.; Kumar, S.A.; Alhamami, M.A.; Almehbad, N. Exploring the Potential of Reduced Graphene Oxide/Polyaniline (rGO@ PANI) Nanocomposites for High-Performance Supercapacitor Application. *Electrochim. Acta* **2024**, *479*, 143743. [CrossRef]
17. Liu, Y.; Wang, Z.; Zhong, Y.; Xu, X.; Veder, J.-P.M.; Rowles, M.R.; Saunders, M.; Ran, R.; Shao, Z. Activation-Free Supercapacitor Electrode Based on Surface-Modified  $\text{Sr}_2\text{CoMo}_{1-x}\text{Ni}_x\text{O}_{6-\delta}$  Perovskite. *Chem. Eng. J.* **2020**, *390*, 124645. [CrossRef]
18. Cao, Y.; Liang, J.; Li, X.; Yue, L.; Liu, Q.; Lu, S.; Asiri, A.M.; Hu, J.; Luo, Y.; Sun, X. Recent Advances in Perovskite Oxides as Electrode Materials for Supercapacitors. *Chem. Commun.* **2021**, *57*, 2343–2355. [CrossRef]
19. Nguyen, T.; Montemor, M.D.F. Metal Oxide and Hydroxide-Based Aqueous Supercapacitors: From Charge Storage Mechanisms and Functional Electrode Engineering to Need-Tailored Devices. *Adv. Sci.* **2019**, *6*, 1801797. [CrossRef]
20. Mei, P.; Kaneti, Y.V.; Pramanik, M.; Takei, T.; Dag, Ö.; Sugahara, Y.; Yamauchi, Y. Two-Dimensional Mesoporous Vanadium Phosphate Nanosheets through Liquid Crystal Templating Method toward Supercapacitor Application. *Nano Energy* **2018**, *52*, 336–344. [CrossRef]
21. Ji, Q.; Bi, L.; Zhang, J.; Cao, H.; Zhao, X.S. The Role of Oxygen Vacancies of  $\text{ABO}_3$  Perovskite Oxides in the Oxygen Reduction Reaction. *Energy Environ. Sci.* **2020**, *13*, 1408–1428. [CrossRef]
22. Agarwal, A.; Sankapal, B.R. Metal Phosphides: Topical Advances in the Design of Supercapacitors. *J. Mater. Chem. A* **2021**, *9*, 20241–20276. [CrossRef]
23. Liu, Y.; Jiang, S.P.; Shao, Z. Intercalation Pseudocapacitance in Electrochemical Energy Storage: Recent Advances in Fundamental Understanding and Materials Development. *Mater. Today Adv.* **2020**, *7*, 100072. [CrossRef]
24. Wu, M.-C.; Chen, W.-C.; Chan, S.-H.; Su, W.-F. The Effect of Strontium and Barium Doping on Perovskite-Structured Energy Materials for Photovoltaic Applications. *Appl. Surf. Sci.* **2018**, *429*, 9–15. [CrossRef]
25. Adimule, V.; Bhat, V.S.; Yallur, B.C.; Gowda, A.H.; Padova, P.D.; Hegde, G.; Toghan, A. Facile Synthesis of Novel  $\text{SrO}_{0.5} \cdot \text{MnO}_{0.5}$  Bimetallic Oxide Nanostructure as a High-Performance Electrode Material for Supercapacitors. *Nanomater. Nanotechnol.* **2022**, *12*, 184798042110640. [CrossRef]
26. Liu, G.F.; Ma, P.P.; Qiao, Y.; Xu, R.H.; Hu, R.Y.; Liu, L.Y.; Jiang, G.H.; Demir, M. Perovskite  $\text{SrCo}_{1-x}\text{TixO}_{3-\delta}$  as Anion-Intercalated Electrode Materials for Supercapacitors. *J. Energy Storage* **2022**, *52*, 104942. [CrossRef]
27. Salas, M.A.S.; De Paoli, J.M.; Pérez, O.E.L.; Bajales, N.; Fuertes, V.C. Synthesis and Characterization of Alumina-Embedded  $\text{SrCo}_{0.95}\text{V}_{0.05}\text{O}_3$  Nanostructured Perovskite: An Attractive Material for Supercapacitor Devices. *Microporous Mesoporous Mater.* **2020**, *293*, 109797. [CrossRef]
28. Ahangari, M.; Mostafaei, J.; Sayyah, A.; Mahmoudi, E.; Asghari, E.; Coruh, A.; Delibas, N.; Niaezi, A. Investigation of Structural and Electrochemical Properties of  $\text{SrFe}_x\text{Co}_{1-x}\text{O}_{3-\delta}$  Perovskite Oxides as a Supercapacitor Electrode Material. *J. Energy Storage* **2023**, *63*, 107034. [CrossRef]
29. Qiao, Y.; Liu, G.; Xu, R.; Hu, R.; Liu, L.; Jiang, G.; Demir, M.; Ma, P.  $\text{SrFe}_{1-x}\text{Zr}_x\text{O}_{3-\delta}$  Perovskite Oxides as Negative Electrodes for Supercapacitors. *Electrochim. Acta* **2023**, *437*, 141527. [CrossRef]
30. Mendoza, R.; Oliva, J.; Padmasree, K.P.; Mtz-Enriquez, A.I.; Zakhidov, A.; Encinas, A. Using the Amorphous-Carbon Derived from Cigarette Filters for the Fabrication of Highly Efficient Flexible Supercapacitors and Role of the  $\text{Sr}_{3.2}\text{Y}_{0.8}\text{Fe}_{1.5}\text{Co}_{1.5}\text{O}_{10}$  Layered Perovskite to Enhance Their Electrochemical Performance. *J. Energy Storage* **2023**, *60*, 106539. [CrossRef]
31. Maheswari, N.; Muralidharan, G. Supercapacitor Behavior of Cerium Oxide Nanoparticles in Neutral Aqueous Electrolytes. *Energy Fuels* **2015**, *29*, 8246–8253. [CrossRef]
32. Ansari, A.A.; Adil, S.F.; Alam, M.; Ahmad, N.; Assal, M.E.; Labis, J.P.; Alwarthan, A. Catalytic Performance of the Ce-Doped  $\text{LaCoO}_3$  Perovskite Nanoparticles. *Sci. Rep.* **2020**, *10*, 15012. [CrossRef]
33. Mohan, M.; Shetti, N.P.; Aminabhavi, T.M. Perovskites: A New Generation Electrode Materials for Storage Applications. *J. Power Sources* **2023**, *574*, 233166. [CrossRef]
34. Liu, Z.; Li, L.; Chen, J.; Yang, H.; Xia, L.; Chen, J.; Duan, J.; Chen, Z. Effects of Chelating Agents on Electrochemical Properties of  $\text{Na}_{0.9}\text{Ni}_{0.45}\text{Mn}_{0.55}\text{O}_2$  Cathode Materials. *J. Alloys Compd.* **2021**, *855*, 157485. [CrossRef]

35. Priyadharsini, N.; Kasturi, P.R.; Shanmugavani, A.; Surendran, S.; Shanmugapriya, S.; Selvan, R.K. Effect of Chelating Agent on the Sol-Gel Thermolysis Synthesis of LiNiPO<sub>4</sub> and Its Electrochemical Properties for Hybrid Capacitors. *J. Phys. Chem. Solids* **2018**, *119*, 183–192. [[CrossRef](#)]
36. Kumar, Y.A.; Kumar, K.D.; Kim, H.-J. Facile Preparation of a Highly Efficient NiZn<sub>2</sub>O<sub>4</sub>-NiO Nanoflower Composite Grown on Ni Foam as an Advanced Battery-Type Electrode Material for High-Performance Electrochemical Supercapacitors. *Dalton Trans.* **2020**, *49*, 3622–3629. [[CrossRef](#)] [[PubMed](#)]
37. Kumar, R.D.; Kumar, A.J.; Balachandran, S.; Kusmartsev, F.V.; Trabelsi, A.B.G.; Alkallas, F.H.; Nagarani, S.; Sethuraman, V.; Lee, B.-K. High-Performance Chrysanthemum Flower-like Structure of Ni Doped ZnO Nanoflowers for Pseudo-Supercapacitors. *J. Energy Storage* **2023**, *72*, 108441. [[CrossRef](#)]
38. Fazal, A.; Iqbal, M.J.; Raza, M.A.; Almutairi, B.S.; Iqbal, M.Z.; Subhani, T.; Riaz, S.; Naseem, S. Binder-Free Hydrothermal Approach to Fabricate High-Performance Zinc Phosphate Electrode for Energy Storage Applications. *Ceram. Int.* **2024**, *50*, 2742–2753. [[CrossRef](#)]
39. Hekmat, F.; Hosseini, H.; Shahrokhan, S.; Unalan, H.E. Hybrid Energy Storage Device from Binder-Free Zinc-Cobalt Sulfide Decorated Biomass-Derived Carbon Microspheres and Pyrolyzed Polyaniline Nanotube-Iron Oxide. *Energy Storage Mater.* **2020**, *25*, 621–635. [[CrossRef](#)]
40. Zhao, F.; Xie, D.; Song, X.; Wu, H.; Zhang, Q.; Zou, J.; Zeng, X. Construction of Hydrangea-like Nickel Cobalt Sulfide through Efficient Microwave-Assisted Approach for Remarkable Supercapacitors. *Appl. Surf. Sci.* **2021**, *539*, 148260. [[CrossRef](#)]
41. Tummino, M.L.; Liotta, L.F.; Magnacca, G.; Lo Faro, M.; Trocino, S.; Campagna Zignani, S.; Aricò, A.S.; Deganello, F. Sucrose-Assisted Solution Combustion Synthesis of Doped Strontium Ferrate Perovskite-Type Electrocatalysts: Primary Role of the Secondary Fuel. *Catalysts* **2020**, *10*, 134. [[CrossRef](#)]
42. Tummino, M.L.; Vineis, C.; Varesano, A.; Liotta, L.F.; Rigoleto, M.; Laurenti, E.; Deganello, F. Sr<sub>0.85</sub>Ce<sub>0.15</sub>Fe<sub>0.67</sub>Co<sub>0.33-x</sub>Cu<sub>x</sub>O<sub>3</sub> Perovskite Oxides: Effect of B-Site Copper Codoping on the Physicochemical, Catalytic and Antibacterial Properties upon UV or Thermal Activation. *Front. Environ. Eng.* **2023**, *2*, 1249931. [[CrossRef](#)]
43. Deganello, F.; Liotta, L.F.; Leonardi, S.G.; Neri, G. Electrochemical Properties of Ce-Doped SrFeO<sub>3</sub> Perovskites-Modified Electrodes towards Hydrogen Peroxide Oxidation. *Electrochim. Acta* **2016**, *190*, 939–947. [[CrossRef](#)]
44. Tummino, M.L.; Laurenti, E.; Deganello, F.; Prevot, A.B.; Magnacca, G. Revisiting the Catalytic Activity of a Doped SrFeO<sub>3</sub> for Water Pollutants Removal: Effect of Light and Temperature. *Appl. Catal. B Environ.* **2017**, *207*, 174–181. [[CrossRef](#)]
45. Markov, A.A.; Nikitin, S.S.; Leonidov, I.A.; Patrakeev, M.V. Oxygen and Electron Transport in Ce<sub>0.1</sub>Sr<sub>0.9</sub>FeO<sub>3-δ</sub>. *Solid. State Ion.* **2020**, *344*, 115131. [[CrossRef](#)]
46. Wei, Y.; Gui, H.; Zhao, Z.; Li, J.; Liu, Y.; Xin, S.; Li, X.; Xie, W. Structure and Magnetic Properties of the Perovskite YCo<sub>0.5</sub>Fe<sub>0.5</sub>O<sub>3</sub>. *AIP Adv.* **2014**, *4*, 127134. [[CrossRef](#)]
47. Yao, C.; Zhang, H.; Liu, X.; Meng, J.; Meng, F. A Niobium and Tungsten Co-Doped SrFeO<sub>3-δ</sub> Perovskite as Cathode for Intermediate Temperature Solid Oxide Fuel Cells. *Ceram. Int.* **2019**, *45*, 7351–7358. [[CrossRef](#)]
48. Palenik, R.C.; Abboud, K.A.; Palenik, G.J. Bond Valence Sums and Structural Studies of Antimony Complexes Containing Sb Bonded Only to O Ligands. *Inorganica Chim. Acta* **2005**, *358*, 1034–1040. [[CrossRef](#)]
49. Talaei, M.; Hassanzadeh-Tabrizi, S.A.; Saffar-Teluri, A. Synthesis of Mesoporous CuFe<sub>2</sub>O<sub>4</sub>@SiO<sub>2</sub> Core-Shell Nanocomposite for Simultaneous Drug Release and Hyperthermia Applications. *Ceram. Int.* **2021**, *47*, 30287–30297. [[CrossRef](#)]
50. Aydoghmis, S.M.; Hassanzadeh-Tabrizi, S.A.; Saffar-Teluri, A. Facile Synthesis and Investigation of NiO-ZnO-Ag Nanocomposites as Efficient Photocatalysts for Degradation of Methylene Blue Dye. *Ceram. Int.* **2019**, *45*, 14934–14942. [[CrossRef](#)]
51. Pecchi, G.; Campos, C.; Peña, O. Thermal Stability against Reduction of LaMn<sub>1-y</sub>CoyO<sub>3</sub> Perovskites. *Mater. Res. Bull.* **2009**, *44*, 846–853. [[CrossRef](#)]
52. Zheng, X.; Li, B.; Shen, L.; Cao, Y.; Zhan, Y.; Zheng, S.; Wang, S.; Jiang, L. Oxygen Vacancies Engineering of Fe Doped LaCoO<sub>3</sub> Perovskite Catalysts for Efficient H<sub>2</sub>S Selective Oxidation. *Appl. Catal. B Environ.* **2023**, *329*, 122526. [[CrossRef](#)]
53. Asaithambi, S.; Sakthivel, P.; Karuppaiah, M.; Yuvakkumar, R.; Balamurugan, K.; Ahamad, T.; Khan, M.M.; Ramalingam, G.; Mohammed, M.K.; Ravi, G. Preparation of Fe-SnO<sub>2</sub>@CeO<sub>2</sub> Nanocomposite Electrode for Asymmetric Supercapacitor Device Performance Analysis. *J. Energy Storage* **2021**, *36*, 102402. [[CrossRef](#)]
54. Manju; Jain, M.; Madas, S.; Vashishtha, P.; Rajput, P.; Gupta, G.; Kahaly, M.U.; Özdogan, K.; Vij, A.; Thakur, A. Oxygen Vacancies Induced Photoluminescence in SrZnO<sub>2</sub> Nanophosphors Probed by Theoretical and Experimental Analysis. *Sci. Rep.* **2020**, *10*, 17364.
55. Suggana, P.; Kumar, E.P.; Reddy, K.C.; Lakshmaiah, M.V.; Joo, S.W.; Reddy, G.R. 2D Sheet to 1D Rod-like Morphology Regulated Self-Assembled ZnCo<sub>2</sub>O<sub>4</sub> Microstructures under Mixed Solvent Conditions for Battery-Type Supercapacitors. *Colloids Surf. A Physicochem. Eng. Asp.* **2023**, *669*, 131423. [[CrossRef](#)]
56. Seenivasan, S.; Shim, K.I.; Lim, C.; Kavinkumar, T.; Sivagurunathan, A.T.; Han, J.W.; Kim, D.-H. Boosting Pseudocapacitive Behavior of Supercapattery Electrodes by Incorporating a Schottky Junction for Ultrahigh Energy Density. *Nano-Micro Lett.* **2023**, *15*, 62. [[CrossRef](#)]

57. Liang, M.; Zhao, M.; Wang, H.; Shen, J.; Song, X. Enhanced Cycling Stability of Hierarchical  $\text{NiCo}_2\text{S}_4@ \text{Ni(OH)}_2@ \text{PPy}$  Core–Shell Nanotube Arrays for Aqueous Asymmetric Supercapacitors. *J. Mater. Chem. A* **2018**, *6*, 2482–2493. [[CrossRef](#)]
58. William, J.J.; Balakrishnan, S.; Murugesan, M.; Gopalan, M.; Britten, A.J.; Mkandawire, M. Mesoporous  $\beta\text{-Ag}_2\text{MoO}_4$  Nanopotaatoes as Supercapacitor Electrodes. *Mater. Adv.* **2022**, *3*, 8288–8297. [[CrossRef](#)]
59. Safari, M.; Mazloom, J.; Boustani, K.; Monemdjou, A. Hierarchical  $\text{Fe}_2\text{O}_3$  Hexagonal Nanoplatelets Anchored on  $\text{SnO}_2$  Nanofibers for High-Performance Asymmetric Supercapacitor Device. *Sci. Rep.* **2022**, *12*, 14919. [[CrossRef](#)]
60. Ahangari, M.; Mahmoodi, E.; Delibaş, N.; Mostafaei, J.; Asghari, E.; Niaezi, A. Application of  $\text{SrFeO}_3$  Perovskite as Electrode Material for Supercapacitor and Investigation of Co-Doping Effect on the B-Site. *Turk. J. Chem.* **2022**, *46*, 1723–1732. [[CrossRef](#)]
61. Liu, L.; Liu, G.; Wu, S.; He, J.; Zhou, Y.; Demir, M.; Huang, R.; Ruan, Z.; Jiang, G.; Ma, P. Fe-Substituted  $\text{SrCoO}_3$  Perovskites as Electrode Materials for Wide Temperature-Tolerant Supercapacitors. *Ceram. Int.* **2024**, *50*, 1970–1980. [[CrossRef](#)]
62. Shafi, P.M.; Mohapatra, D.; Reddy, V.P.; Dhakal, G.; Kumar, D.R.; Tuma, D.; Brousse, T.; Shim, J.-J. Sr-and Fe-Substituted  $\text{LaMnO}_3$  Perovskite: Fundamental Insight and Possible Use in Asymmetric Hybrid Supercapacitor. *Energy Storage Mater.* **2022**, *45*, 119–129. [[CrossRef](#)]
63. George, G.; Jackson, S.L.; Luo, C.Q.; Fang, D.; Luo, D.; Hu, D.; Wen, J.; Luo, Z. Effect of Doping on the Performance of High-Crystalline  $\text{SrMnO}_3$  Perovskite Nanofibers as a Supercapacitor Electrode. *Ceram. Int.* **2018**, *44*, 21982–21992. [[CrossRef](#)]
64. Tomar, A.K.; Singh, G.; Sharma, R.K. Fabrication of a Mo-Doped Strontium Cobaltite Perovskite Hybrid Supercapacitor Cell with High Energy Density and Excellent Cycling Life. *ChemSusChem* **2018**, *11*, 4123–4130. [[CrossRef](#)] [[PubMed](#)]
65. Ajin, I.; Balamurugan, R.; Chandra Bose, A. Tailoring the Perovskite Structure to Acquire an Inorganic  $\text{La}_2\text{NiCrO}_6$  Double Perovskite as an Efficient Energy Storage Application by Varying Molar Concentrations of Citric Acid. *ACS Appl. Energy Mater.* **2023**, *6*, 9764–9777. [[CrossRef](#)]
66. Zhang, Y.; Ding, J.; Xu, W.; Wang, M.; Shao, R.; Sun, Y.; Lin, B. Mesoporous  $\text{LaFeO}_3$  Perovskite Derived from MOF Gel for All-Solid-State Symmetric Supercapacitors. *Chem. Eng. J.* **2020**, *386*, 124030. [[CrossRef](#)]
67. Raj, T.V.; Hoskeri, P.A.; Muralidhara, H.B.; Manjunatha, C.R.; Kumar, K.Y.; Raghu, M.S. Facile Synthesis of Perovskite Lanthanum Aluminate and Its Green Reduced Graphene Oxide Composite for High Performance Supercapacitors. *J. Electroanal. Chem.* **2020**, *858*, 113830. [[CrossRef](#)]

**Disclaimer/Publisher’s Note:** The statements, opinions and data contained in all publications are solely those of the individual author(s) and contributor(s) and not of MDPI and/or the editor(s). MDPI and/or the editor(s) disclaim responsibility for any injury to people or property resulting from any ideas, methods, instructions or products referred to in the content.